X-ray spectro-microscopy of complex materials and surfaces

by J. Stöhr
S. Anders

The detailed understanding of complex materials used in information technology requires the use of state-of-the-art experimental techniques that provide information on the electronic and magnetic properties of the materials. The increasing miniaturization of components furthermore demands the use of techniques with spatial resolution down to the nanometer range. A means to satisfy both requirements is to combine the capabilities of conventional X-ray absorption spectroscopy with those of electron microscopy in a new technique designated as X-ray photoemission electron microscopy. This paper reviews the principles of this new spectro-microscopy approach and presents selected applications to the study of materials of interest in information technology.

Introduction

The characterization of advanced materials and their surfaces and the understanding of their properties can lead to improvements or even redirections of technological processes used in information technology. Today, the pursuit of such understanding demands the development of new techniques that are capable of providing information about composition and crystallographic structure, as well as electronic and magnetic structure, on a length scale that is small compared to the size of lithographically fabricated structures ($<0.3\ \mu$m). In many cases, information is sought on an even smaller scale—the crystallographic grain size of materials (about 20 nm).

The spectro-microscopy approach [1, 2], described here, combines two well-established concepts in an attempt to reach the ultimate goal of obtaining element-specific electronic and magnetic information on the atomic scale. One pillar of the new spectro-microscopy approach is the well-established technique of polarized X-ray absorption spectroscopy [3, 4] which provides information on *composition* through its elemental specificity, on the *local bonding environments of the atoms* through its chemical specificity (binding energy shifts) and structural sensitivity (absorption fine structure), and on the *orientation and size of magnetic moments* through polarization-dependent effects (linear [5] and circular [6] magnetic dichroism). The other pillar is provided by the well-known capability of full-field imaging by the use of an electron microscope [7], in our case using the secondary photoelectrons that are emitted after X-ray absorption as the signal [1, 2].

This review covers the principles and capabilities of X-ray photoemission electron microscopy (XPEEM). In particular, it describes an instrument, PEEM2, developed by IBM in conjunction with the Lawrence Berkeley National Laboratory and Arizona State University that is installed on a soft-X-ray beamline at the Advanced Light Source (ALS) [8] facility in Berkeley. Various examples are then given to illustrate the capabilities of the XPEEM technique. The examples address materials issues encountered in various areas such as storage technology and semiconductor processing.

©**Copyright** 2000 by International Business Machines Corporation. Copying in printed form for private use is permitted without payment of royalty provided that (1) each reproduction is done without alteration and (2) the *Journal* reference and IBM copyright notice are included on the first page. The title and abstract, but no other portions, of this paper may be copied or distributed royalty free without further permission by computer-based and other information-service systems. Permission to *republish* any other portion of this paper must be obtained from the Editor.

0018-8646/00/$5.00 © 2000 IBM

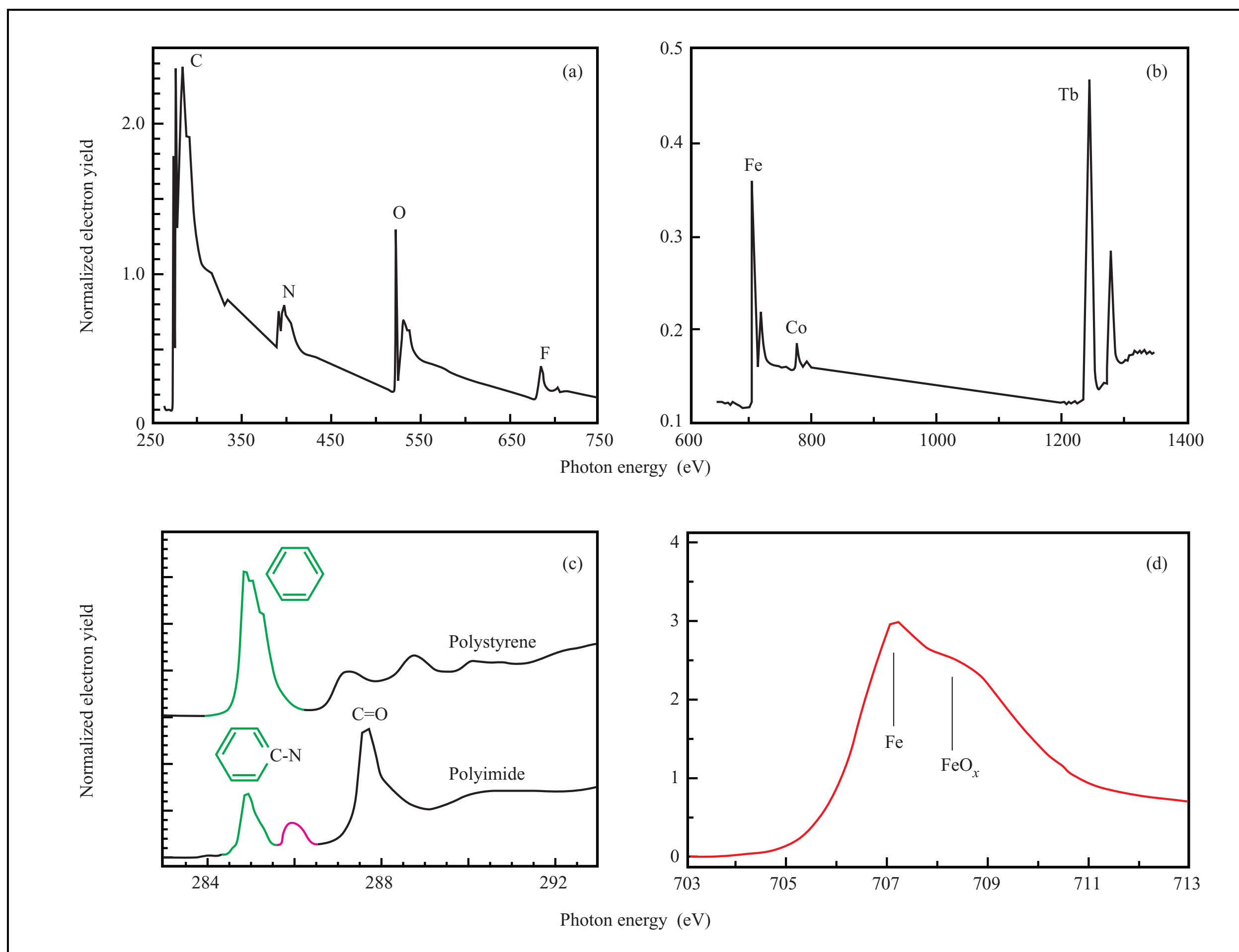

Figure 1

Information content in X-ray absorption spectra. Elemental specificity is illustrated by spectra recorded for a polyimide polymer (a) and a $Tb_{24.5}Fe_{70.5}Co_{5.0}$ magnetic alloy (b), as discussed in the text. Chemical specificity is illustrated by the NEXAFS spectra of polystyrene and polyimide (c), which clearly show resonances associated with the phenyl and N–C=O groups [9], and by the spectrum of a slightly oxidized Fe film (d).

Concepts of spectroscopy and microscopy

- *X-ray absorption spectroscopy*

Some of the most powerful spectroscopy methods are based on the absorption of photons, since this process is guided by simple electronic dipole transitions. X-ray spectroscopy offers an advantage over visible-light spectroscopy because it is element-specific. The specificity arises from the characteristic binding energies of the atomic core electrons, as illustrated in **Figures 1(a)** and **1(b)** for polymers and transition metals, respectively. The soft-X-ray absorption spectrum directly exhibits the characteristic absorption edges of the elements in the sample, as shown for a polyimide polymer in Figure 1(a) and for a $Tb_{24.5}Fe_{70.5}Co_{5.0}$ alloy in Figure 1(b). At the absorption thresholds of the elements, such spectra show strong resonances arising from transitions to unfilled valence states. In the case of polymers, these states are unfilled molecular orbitals, while in the case of transition metals, the states correspond to the unfilled valence band. Since the transitions are governed by the $\Delta l = \pm 1$ selection rule, polymers are studied using K-edges ($1s \rightarrow 2p$ transitions), transition metals are best studied using $L_{2,3}$-edges ($2p \rightarrow 3d$ transitions), and rare earths using $M_{4,5}$-edges ($3d \rightarrow 4f$ transitions), as shown in Figures 1(a) and 1(b). X-ray absorption spectroscopy, like XPS, is also sensitive to the chemical environment. This is illustrated in **Figure 1(c)**, which shows the different near-edge fine

structures of two polymers, polyimide and polystyrene, and in **Figure 1(d)**, where the fine structure at the L_3-edge of an oxidized Fe film is shown.

In practice, X-ray absorption spectroscopy is carried out with polarized synchrotron radiation. For a bending magnet source, used for the experiments in this paper, the polarization of the X-rays is simply changed by means of an aperture from left or right circular to linear [2]. It is well known that linearly polarized X-rays can be used to probe the orientation of molecular orbitals. This is one of the strengths of near-edge X-ray absorption fine-structure (NEXAFS) spectroscopy [4]. An example is given in **Figure 2(a)**, where the polarization-dependent X-ray absorption spectrum of a rubbed polyimide sample is shown. Such materials are used as liquid crystal alignment layers in IBM's flat-panel displays. The NEXAFS spectra in Figure 2(a) clearly show strong changes upon alignment of the electric field vector parallel instead of perpendicular to the rubbing direction. This is due to the preferential orientation of the molecular chains and functional groups at the polymer surface induced by the rubbing process [9]. More generally, polarized X-ray absorption can sense the charge anisotropy of the valence states involved in the core excitation process [10, 11]. The electric field vector of the linearly polarized X-rays acts as a "searchlight" for the number of valence holes in different directions of the atomic volume. In most cases the anisotropy of the charge in the atomic volume is caused by an anisotropy in the bonding, as for the rubbed polyimide of Figure 2(a). For magnetic materials, however, the alignment of the local atomic spins can also cause an anisotropy in the charge through the spin-orbit coupling. For example, in a cubic material the charge is highly isotropic in the atomic sphere, but in the presence of a magnetic interaction it shows a small ellipse-like distortion about the magnetic direction. This charge anisotropy leads to an asymmetry of the X-ray absorption signal through the searchlight effect. This so-called X-ray magnetic linear dichroism (XMLD) spectroscopy [5] provides a powerful method by which to determine the direction of the magnetic axis in antiferromagnets, as illustrated in **Figure 2(b)** for antiferromagnetic fcc NiO. Here the intensity of the multiplet peaks at the Ni L_2 absorption edge depends on whether the electric field vector is aligned parallel or perpendicular to the antiferromagnetic axis [12].

Circularly polarized X-rays are particularly useful for the study of ferromagnets or ferrimagnets, i.e., systems with a net magnetic moment. In order to measure the difference in the number of d holes with up and down spin (the magnetic moment), we must make the X-ray absorption process spin-dependent. This is done by the use of right or left circularly polarized photons which transfer their angular momentum (photon spin) to the

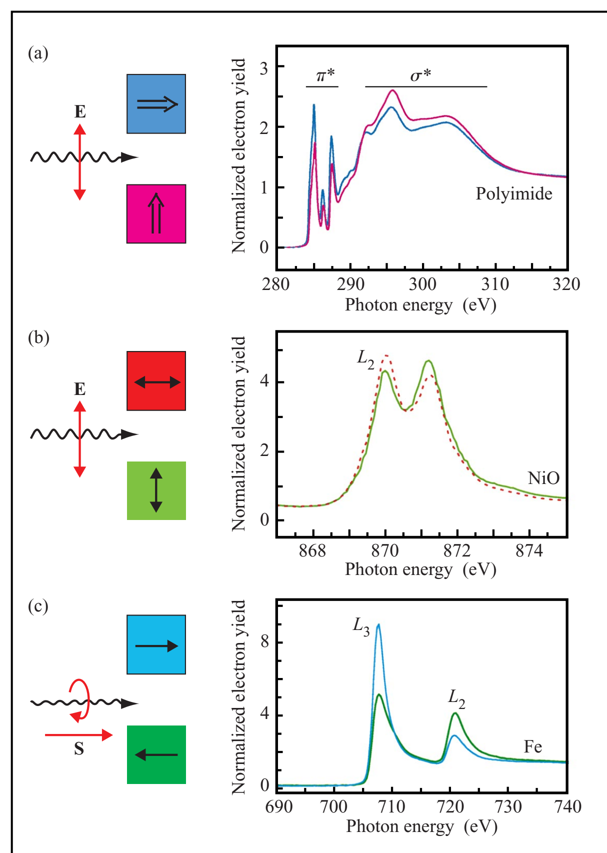

Figure 2

Illustration of various polarization effects in X-ray absorption spectra: (a) X-ray linear dichroism caused by the preferential bond orientation in rubbed BPDA–PDA polyimide films relative to the X-ray electric field vector [9]. (b) X-ray magnetic linear dichroism caused by preferential orientation of the antiferromagnetic axis at the surface of NiO(100) films grown on MgO(100) relative to the X-ray electric field vector [2, 12]. (c) X-ray magnetic circular dichroism caused by unidirectional orientation of the magnetic moment in a magnetized film of Fe metal relative to the photon helicity [2, 16].

excited photoelectrons. The maximum dichroism effect in X-ray magnetic circular dichroism (XMCD) spectroscopy [6] is observed if the photon spin direction and the magnetization directions are parallel and antiparallel, as shown in **Figure 2(c)**. When the photon spin and the magnetization directions are perpendicular, the resonance intensities at the L_3 and L_2 edges lie between those shown in Figure 2(c) for parallel and antiparallel alignments. The differences in the intensities at the L_3 and L_2 edges for parallel and antiparallel orientation of photon spin and magnetization directions are quantitatively related by sum rules to the size of the spin and orbital magnetic moments and to the anisotropies of the spin density and orbital moment [13–15]. XMCD spectroscopy can therefore

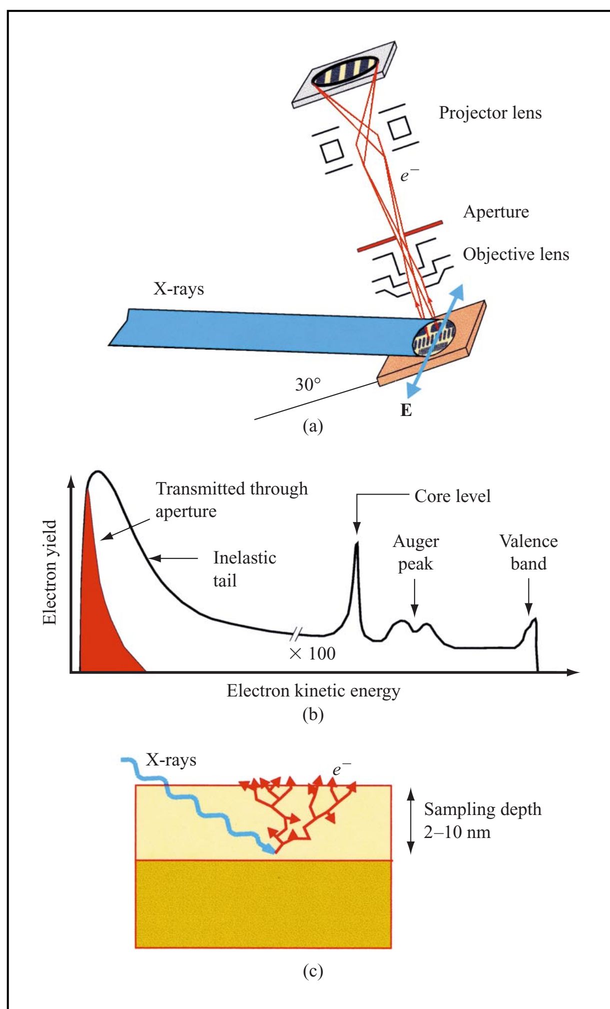

Figure 3

(a) Schematic of the experimental arrangement used in photoemission electron microscopy. The X-ray beam is incident on the sample at a grazing angle of 30° and forms a focused spot about 30 μm wide. The emitted photoelectrons are imaged by an all-electrostatic electron optics system onto a phosphor screen that is read by a CCD camera. (b) Schematic energy distribution of the emitted photoelectrons. The aperture in the PEEM microscope in (a) leads to an energy-filtering effect, so that only the secondary-electron intensity shown in red is transmitted. (c) Illustration of the scattering events of the secondary electrons leading to an effective sampling depth in the range 2–10 nm, depending on the material being examined.

determine the sizes, the directions, and anisotropies (sizes in different directions) of the atomic magnetic moments, as reviewed previously [11, 16].

- *Photoemission electron microscopy*

The two basic requirements for microscopy are spatial resolution and contrast; we discuss them in turn below. As in electron microscopy, one can use scanning or imaging methods to obtain spatial resolution; this has been discussed elsewhere [2]. A particularly powerful imaging method, illustrated in **Figure 3**, is based on a combination of X-ray and electron techniques [1, 2, 8]. The sample is illuminated by a monochromatic X-ray beam that is only moderately focused, e.g., to tens of micrometers, so that it matches the maximum field of view of a photoemission electron microscope. The energy resolution for spectroscopy is determined by the X-ray monochromator in the beamline, and the spatial resolution for microscopy is determined by the electron optics in the photoemission electron microscope (PEEM). It is limited by three quantities: spherical aberration, chromatic aberration, and diffraction. In practice, for X-ray excitation of electrons, chromatic aberrations of the accelerating field between the sample and the electron optics dominate [7, 8, 17]. The aberrations originate from errors in the focusing of electrons having different kinetic energies. The electron intensity is dominated, by orders of magnitude, by the secondary electron tail in the 0–20-eV kinetic energy range, where zero kinetic energy corresponds to the vacuum level of the sample. The large secondary-electron intensity is a direct measure of the X-ray absorption coefficient of the sample as a function of photon energy [4] and conveniently provides a suitably large PEEM signal.

The energy spread of the inelastic tail (about 5 eV for most materials [18]) degrades the lateral resolution through chromatic aberrations. Most PEEM instruments do not incorporate an electron energy analyzer or filter, and their spatial resolution is determined by the effective width of the secondary-electron distribution. Fortunately, the effective width of the energy spread can be reduced by a suitable aperture placed in one of the back focal planes of the PEEM electron optics, as shown in Figure 3(a). The aperture acts as a filter for high-energy electrons which are focused behind the aperture while the low-energy portion of the inelastic tail is properly focused at the aperture position and is thus transmitted. The transmitted portion is schematically shown in red in Figure 3(b). Calculations show that a spatial resolution in the 10–20-nm range can be obtained by X-ray PEEM (XPEEM) because of the energy-filtering effect of the aperture [8, 17]. Even better spatial resolutions are achieved when the energy spread of the emitted electrons is reduced by use of ultraviolet radiation with an energy slightly higher than the work function [7]. In this case, chromatic aberrations are strongly reduced by the narrow width of the secondary-electron distribution, and a spatial resolution of 8 nm has been demonstrated [7]. However, the increased spatial resolution is accompanied by a loss in elemental specificity. In the future, lateral resolutions near 2 nm may become possible with XPEEM through the use of

aberration-correction and/or energy-filtering schemes [19, 20].

The XPEEM electron signal originates close to the sample surface. The sampling depth, illustrated in Figure 3(c), is determined by the cascading process of the scattered Auger electrons created after core excitation. The $1/e$ sampling depth is about 1.7 nm for Fe and 2.5 nm for Co and Ni [21] and, in general, is related to the density of states at the Fermi level. For example, it is larger in the noble metal Ag (~4 nm) [2]. As a rule of thumb one can still "see" layers that are buried as deep as three times the $1/e$ sampling depth.

The intensity changes with photon energy or X-ray polarization discussed in the earlier spectroscopy section naturally lend themselves as contrast mechanisms for X-ray microscopy. The first contrast mechanism is a variation of the electron yield caused by a change in photon energy. For example, if the photon energy is tuned to the L_3 resonance of elemental Fe [see Figure 1(b)], the measured signal from the sample will emphasize Fe over other elements. A photon energy of 707.1 eV will emphasize elemental Fe over FeO_x, which yields a stronger signal at 708.5 eV, as shown in Figure 1(d). The second contrast mechanism is based on X-ray polarization. If we use handed circular polarization, Fe regions in the sample whose magnetization direction is parallel to the photon spin are emphasized [Figure 2(c)]. This was first demonstrated by imaging bits on a magnetic recording disk [22]. In many cases it is not necessary to change the photon spin (polarization) in XMCD microscopy, since the contrast is large and can be enhanced by combining images recorded at the L_3 and L_2 edges which give opposite contrast [see Figure 2(c)] [22]. Linear polarization is useful for imaging regions in the sample with different bond orientations, e.g., in polymers [23, 24] or in antiferromagnetic regions with different orientations of the magnetic axis [25, 26]. For antiferromagnets, the photon energy of the linearly polarized light is tuned to a particular multiplet peak, e.g., one of the L_2-edge peaks in Figure 2(b). Domains with an orientation of the magnetic axis parallel to the electric field vector will then show a different intensity from those with the axis perpendicular to it. Again, the contrast can be enhanced by combining images taken at different photon (multiplet) energies. In addition to the spectroscopic contrast, other basic contrast mechanisms exist.

In XPEEM contrast also arises from the surface topography and differences in the local work function. As illustrated in **Figure 4**, the electric field is distorted at surface topographical features. This leads to a distortion of the electron trajectories, causing peaks to appear darker and valleys brighter than flat regions. In addition, a shadowing effect arises from X-ray illumination at grazing incidence, and surface features which are at a more perpendicular angle to the X-rays will absorb more strongly and appear brighter, while other areas may not be illuminated at all. Local regions with lower work function will give rise to larger electron intensity.

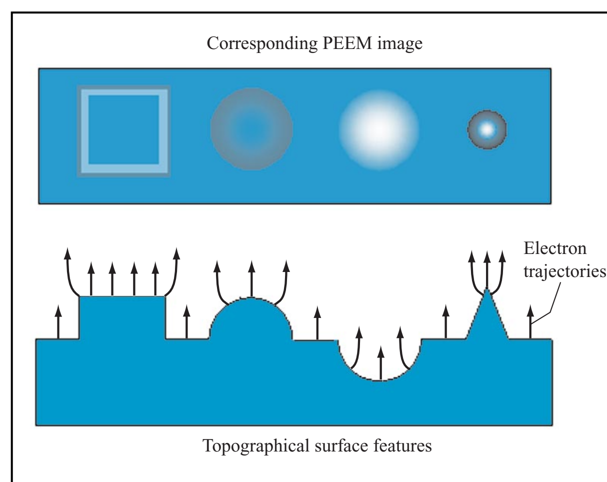

Figure 4

Sources of topographical contrast in PEEM. In the image, topographical peaks of the sample appear darker than its valleys.

PRISM and PEEM2 photoemission electron microscopes

The experiments described in the following sections were performed with two different microscopes. The older PRISM [27] (or PEEM1) microscope is a two-lens, electrostatic microscope operating at a nominal voltage of 10 kV. The microscope, shown schematically in Figure 3(a), is equipped with an aperture at the back focal plane of the objective lens to limit the pencil angle of the electron trajectories and thus increase the resolution. The microscope has a spatial resolution of 200 nm, and it has been described in detail elsewhere [27]. For the present experiments, PRISM was located at the undulator beamline 8.0 of the ALS. The undulator source produces only linearly polarized X-rays, which are monochromatized by a spherical grating monochromator that covers the energy range from 200 to 1500 eV with a high resolving power ($E/\Delta E = 10\,000$).

The PEEM2 photoemission electron microscope is permanently installed on a bending magnet beamline at the ALS. The beamline covers the 175–1500-eV spectral range containing the K-edges of the low-Z elements C, N, O, and F, the L-edges of the $3d$ transition metals, and the $M_{4,5}$-edges of the rare earths. In the horizontal direction, the radiation is focused by an elliptical mirror into a 30-μm-wide spot (at the sample). The photon flux at the

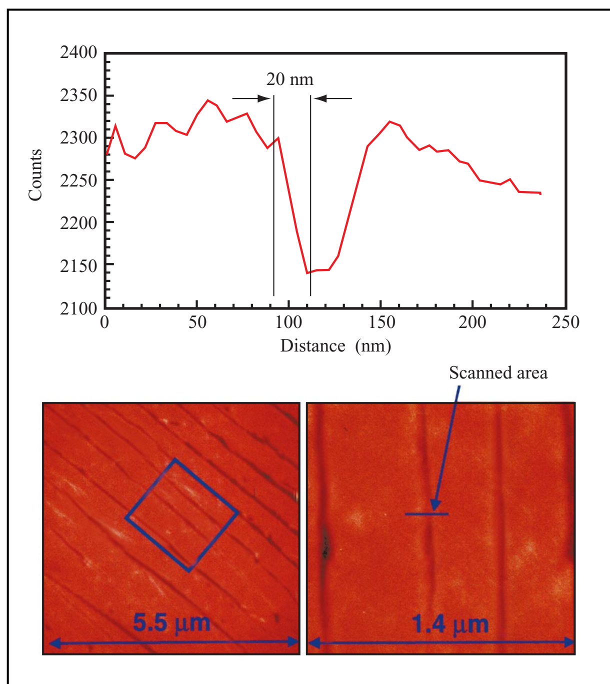

Figure 5

Low- and high-resolution PEEM images of a discharge track on a $LaFeO_3$ sample, obtained via emission from the La M_5 edge. The spatial resolution estimated from the indicated line scan across the high-resolution image is 20 nm. From [8], with permission.

design bandpass ($E/\Delta E = 1800$) of 0.45 eV at 800 eV is 2×10^{12} photons/s in a 30-μm spot with the storage ring operating at 1.9 GeV and a ring current of 400 mA. A mask upstream of the monochromator is used to select above-plane (left circularly polarized), in-plane (linearly polarized), or below-plane (right circularly polarized) radiation.

As illustrated in Figure 3(a), the X-rays are incident on the sample at a 30° angle from the surface, and the optical axis of PEEM2 lies along the surface normal of the sample. For linear polarization, the X-ray electrical field vector lies in the surface plane of the sample. The microscope is an electrostatic system consisting of four lenses to allow for a large range of magnifications. A fiber optic plate serves as the vacuum interface, and the slow-scan CCD camera is directly coupled, using fiber optics, to the fiber optic plate for efficient imaging. The camera accommodates variable exposure times. Typical image-acquisition times are a few seconds to tens of seconds. The operation distance between the objective lens and the sample is about 2 mm, and the maximum operation voltage of PEEM2 is 30 kV. Since in practice many samples show the onset of considerable field emission at operation voltages around 25 kV, destabilizing the image, the typical operation voltage is maintained around 20 kV. The sample as well as the center electrodes of the lenses are maintained at a high negative potential, whereas the detector is maintained at ground potential. It is possible to select certain areas of interest in the image which may be of arbitrary shape and record local NEXAFS spectra of these areas. PEEM2, which is described in detail elsewhere [8], is equipped with a motorized fast sample transfer system connected to a load-lock chamber.

The theoretical resolution limit of a microscope pertains to an ideally flat, conducting sample with large (e.g., elemental) contrast. Many "real-world" samples do not fulfill these conditions, and the resolution depends on sample properties. Insulating samples pose a particular challenge: Sample resistivity and the incident photon flux density determine the voltage that is created by the depletion of electrons from the illuminated area. This voltage may cause a blurring, movement, or pulsation of the image or may be so large that it prevents photoemission. Such charging can be eliminated by capping the sample with a thin (1–2 nm) metallic layer.

The resolution of PEEM2 is illustrated in **Figure 5**. Shown in the figure are low- and high-resolution images of a discharge track on an (uncapped) $LaFeO_3$ sample acquired at the La M_5 edge. The microscope was operated at 23 kV with a 12-μm aperture, and a 60-s exposure time was used. From the indicated line scan across the high-resolution image, we estimate a resolution of 20 nm. This value is very close to the theoretical limit of the microscope for this aperture size and operating voltage [8].

Applications

In the following sections we discuss various applications which are selected primarily from technological areas of interest in information technology.

- *TiSi interconnections*

Titanium disilicide is an interesting material for the semiconductor industry because it has the lowest resistivity of all refractory metal silicides, good thermal stability, and good compatibility with aluminum metallization. It exists in two different phases: One is a metastable C49 base-centered orthorhombic phase with a specific resistivity of 60–90 $\mu\Omega$-cm; the other is a stable face-centered orthorhombic C54 phase with a specific resistivity of 12–15 $\mu\Omega$-cm [28]. The low-resistivity phase is desirable for on-chip device contacts, but it has been found that as dimensions shrink, the high-resistivity phase is preferentially formed [29, 30]. Titanium-disilicide-patterned structures of various dimensions which were deposited on an oxidized Si wafer have been studied using PRISM in order to detect the local differences between the C49 and C54 phases. The NEXAFS spectra of the two phases differ at the onset of

the titanium L_3 edge, as shown in **Figure 6(a)**. The spectral differences are due to the different nearest-neighbor configurations of Ti in the two phases, and they can serve as differentiation contrast in XPEEM [31].

Figures 6(b)–6(d) show a detail of the patterned structure obtained at an X-ray energy below the peak (445.5 eV), at the peak (459 eV), and at the onset of the Ti L_3 edge (455 eV). Below the edge [Figure 6(b)] the titanium pattern appears dark, and at the peak [Figure 6(c)] the pattern appears bright. At 445.5 eV, the onset of the Ti L_3 absorption edge [Figure 6(d)], bright edges and bright tips of the spokes are observed, indicating a difference in bonding structure—the formation of the low-conductivity phase. As can be seen in Figure 6(a), the low-conductivity phase shows stronger absorption at the onset of the titanium L_3 edge; therefore, the secondary-electron emission is higher, and areas of this phase appear brighter in the image. XPEEM can clearly identify the formation of the different phases of titanium disilicide with high spatial resolution. The local chemical changes observed demonstrate that the C49 phase is formed at the tips and at the edges under the same conditions which lead to the formation of the C54 phase in larger structures. The inhibition of the formation of the C54 phase is essential for the use of $TiSi_2$ for ultralarge-scale integration. The experiments are described in detail elsewhere [31].

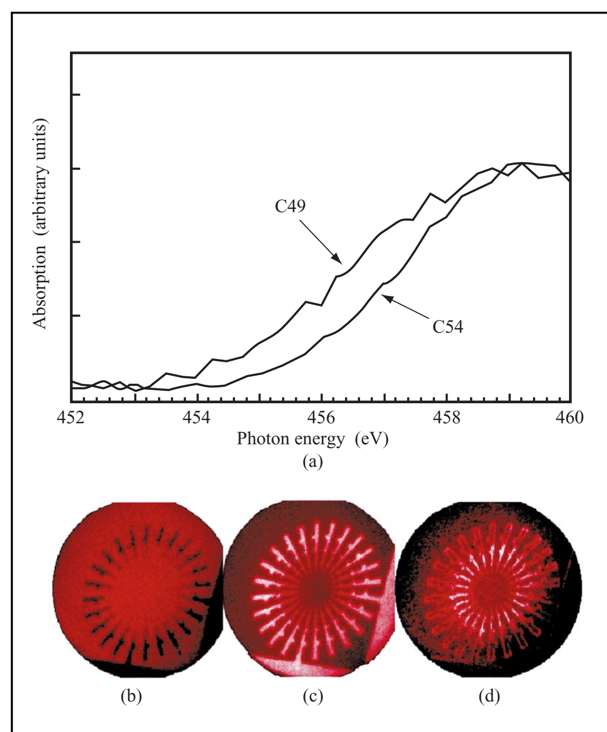

Figure 6

(a) Titanium L_3-edge absorption spectrum for the two phases of titanium disilicide [31]. XPEEM images of the patterned titanium disilicide structure, obtained at X-ray energies (b) below the peak (445.5 eV), (c) at the peak (459 eV), and (d) at the shoulder (455 eV) of the Ti L_3 edge. The spokelike pattern is 80 μm in diameter.

- *Thin-film polymer blends*

Thin films of polymers have considerable technological importance and are used in numerous applications such as color photographic printing, adhesives, paints, or protective coatings. NEXAFS spectroscopy is a powerful tool for the investigation of polymers [4, 32], since the fine structure at the *K*-edges of carbon, nitrogen, and oxygen yields detailed information about the bonding state of the elements and the orientation of their bonds. In many cases blends and bilayers of polymers are used, and the study of associated de-wetting and decomposition phenomena is of considerable importance. Former studies of blends of polystyrene (PS) and partially brominated polystyrene (PBrS) using scanning transmission X-ray microscopy (STXM) and atomic force microscopy (AFM) had revealed a complex morphology which forms as the PS and PBrS phase separate [33] and as thin bilayers de-wet [34]. Information had thus been obtained about the integrated bulk composition of the blends and bilayers and their surface topology, but the chemical state and composition of the surface had remained unknown. We have used the PRISM microscope to study the surface composition of these blends and bilayers.

Blends and bilayers of PS and PBrS on silicon substrates were used for these studies. The blends contained 50% PS and 50% PBrS and had a total thickness of 43 nm; the bilayers consisted of a 30-nm-thick PBrS layer above a 30-nm-thick PS layer. The samples were annealed for different amounts of time at 180°C in a vacuum oven.

NEXAFS spectra of homopolymers show the carbon π^* resonance of PS and the main carbon π^* resonance of PBrS at 285.2 eV, and the C–Br-shifted π^* resonance of PBrS at 286.3 eV [35], as shown in **Figure 7(a)**. XPEEM results for the two-days-annealed sample confirmed the STXM and AFM results showing that the de-wetting process starts locally in small areas. The upper PBrS layer opens in small holes, exposing the underlying PS layer. XPEEM images and local NEXAFS spectra taken in the holes and in adjacent areas showed the characteristic shifted π^* resonance of PBrS outside the holes but not inside [35]. If images are acquired on samples annealed for longer durations, XPEEM shows the same spinodal de-wetting patterns [**Figure 7(b)**] that were also found with optical microscopy, AFM, and STXM. Local NEXAFS spectra acquired in various areas on this sample showed that the surface was composed solely of PS and that PBrS could no longer be found [35]. The contrast in

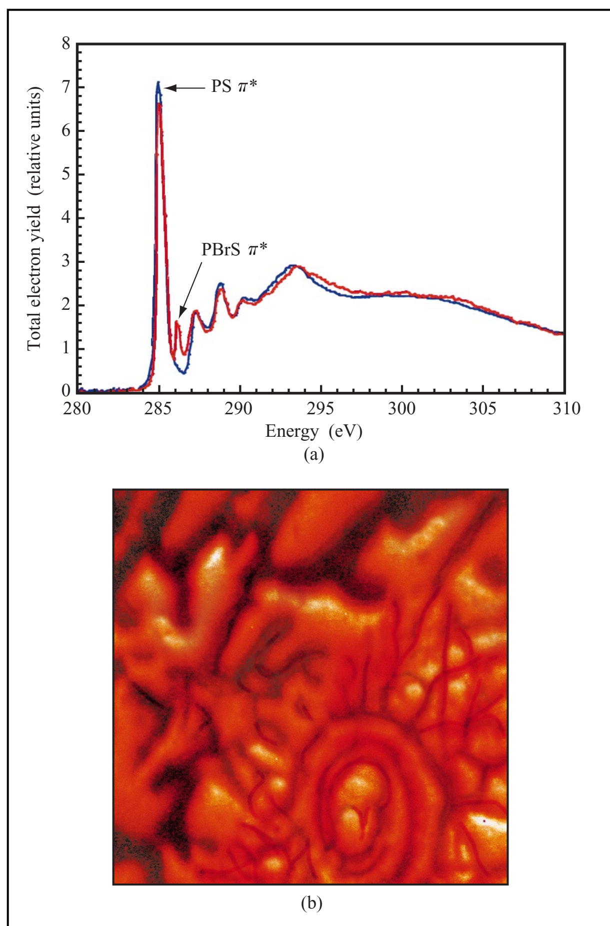

Figure 7

(a) NEXAFS spectra of polystyrene (PS) and brominated polystyrene (PBrS). (b) XPEEM image of a PS/PBrS bilayer obtained at 286.3 eV, after vacuum annealing for four days at 180°C.

Figure 7(b) (acquired at 286.3 eV, the energy of the shifted π^* resonance of PBrS) was only topographical, and no chemical variation at the surface was observed. Bulk-sensitive STXM measurements showed that the integrated composition of the spines consists of PBrS. Our surface-sensitive PRISM results showed that these spines are encapsulated by a thin PS film that covers the entire surface. In blends, it was found that only PS is on the surface even prior to annealing. The blending process initiates the de-wetting and causes the PS to reach the surface and cover it completely [35]. When the thickness of the lower PS was varied, it was observed that full encapsulation of the PBrS by the PS occurs only if the PS is thicker than the radius of gyration of the PS (about 7 nm for 96K molecular weight) [36]. Only partial encapsulation was observed for thinner PS films.

These types of studies allow the investigation of polymer dynamics and provide information about interfacial energies and the relative diffusion and viscosities of polymers in the presence of interfaces.

- *Disk overcoats*

We have also applied the PRISM microscope to study the tribochemical processes at the head/disk interface of magnetic storage media. As a lubricated disk spins beneath a magnetic recording head, the temporary contact of the slider (which contains the magnetic recording head) and the disk can lead to abrasion or chemical reactions at the disk surface, as well as abrasion or the accumulation of debris on the slider. These undesired modifications of the disk and slider surfaces can severely affect the performance of the disk drive, and under a worst-case scenario may lead to a "head crash," with an accompanying loss of stored information. XPEEM is particularly well suited for studies of tribochemical processes because elemental and chemical information can be obtained with high spatial resolution about the status of the surfaces of a disk and its slider before and after wear. The XPEEM investigations were part of a study of the lubricant degradation and decomposition, and detailed results of all of the experiments have been published elsewhere [37–41].

A tribochamber consisting of a spindle, an actuator, and a quadrupole mass spectrometer in UHV (base pressure $<10^{-6}$ Pa) was used for the wear tests [41]. The friction force and the gaseous erosion products of 15 different masses can be monitored simultaneously during a wear test to study the gaseous lubricant erosion products [37]. Supersmooth-textured 65-mm disks were coated with 5-nm-thick cathodic-arc-deposited amorphous hard carbon and lubricated with an 0.85-nm-thick layer of perfluoropolyether (ZDOL) lubricant. Uncoated and coated negative-pressure sliders fabricated from Al_2O_3/TiC were used for the test; the coating was a 6-nm-thick sputter-deposited hydrogenated diamondlike carbon (CH_x). The continuous drag tests were performed at a drag speed of 0.2 m/s, a load of 30 mN, and a sliding time of 600 s. The time between the wear test and the microscopy studies was kept below 2 h to prevent lubricant from flowing back into the wear tracks of the slider.

Figure 8(c) shows an XPEEM image of a wear track on a disk produced by a coated slider. The image was taken at a photon energy of 280 eV, which is below the carbon *K*-edge; therefore, the image contrast is primarily topographical. Local NEXAFS spectra were taken in the undamaged area of the disk, in the wear track caused by the rail of the slider, and in the area between the rails. **Figure 8(a)** shows the carbon *K*-edge spectra and **Figure 8(b)** the fluorine *K*-edge spectra. The carbon

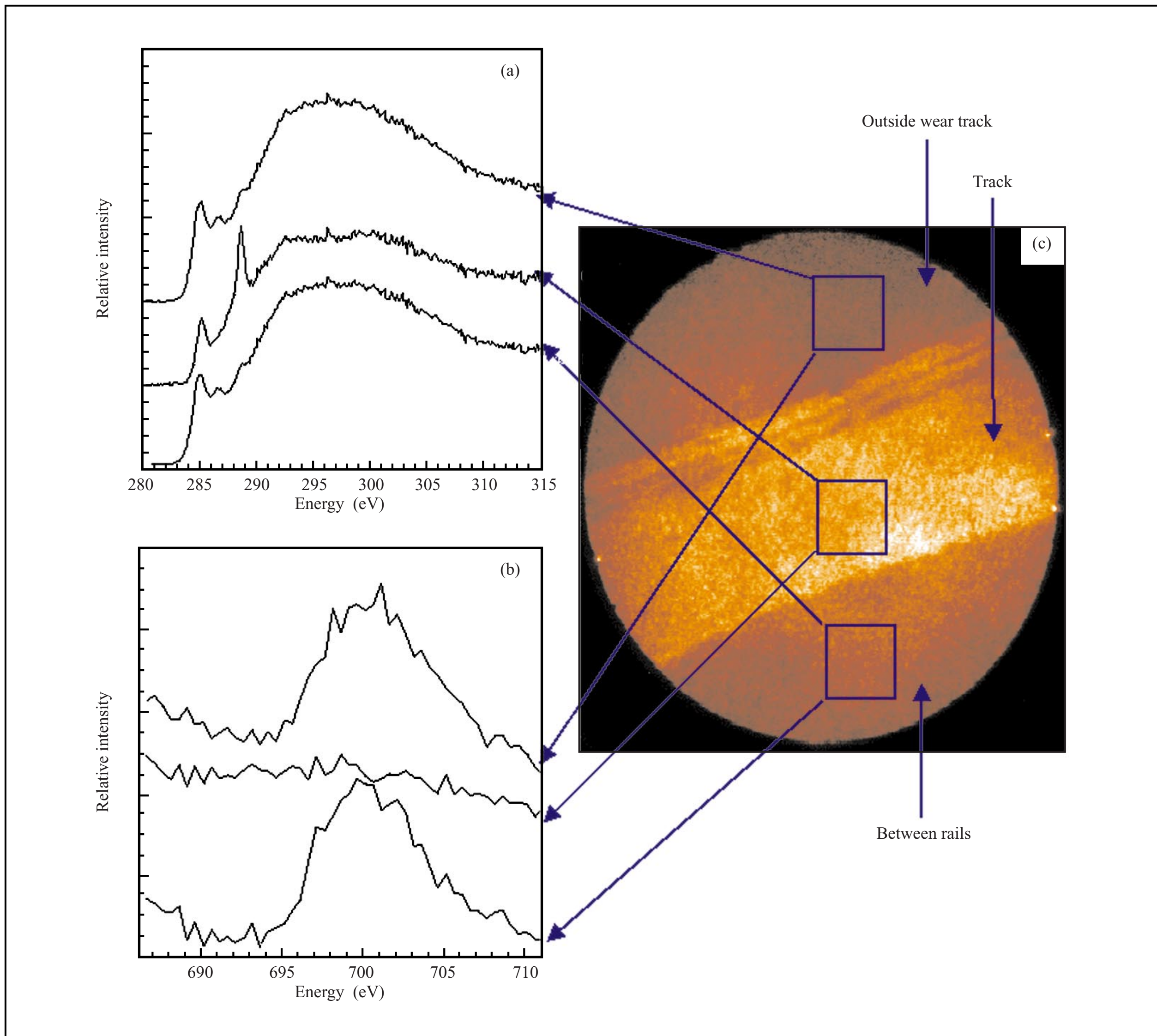

Figure 8

(a) Local carbon *K*-edge NEXAFS spectra of indicated areas. (b) Local fluorine *K*-edge NEXAFS spectra of indicated areas. (c) XPEEM image of a wear track caused by a coated slider on a Z-DOL-lubricated disk taken at a photon energy of 280 eV. The field of view was 150 μm. From [40], with permission.

K-edge spectra are a superposition of signal from the CH_x overcoat and the fluorocarbon lubricant; however, because the lubricant is only about 0.85 nm thick, the NEXAFS signal, originating from a 10-nm probing depth, is dominated by the CH_x overcoat. The spectrum outside the wear track therefore exhibits a typical diamondlike carbon signature, with the π^* resonance at 285 eV corresponding to sp^2-bonded carbon atoms, and the broad σ resonance around 300 eV [4]. The small peak at 286.4 eV can be attributed to C=O bonds [4]. Inside the wear track, an additional strong peak can be observed at 288.5 eV that indicates carboxylic bonds (O=C–OH) [4]. It can also be seen that the total amount of carbon is slightly reduced. In the wear track the fluorine is almost completely removed. Whereas the modified carbon is still visible many weeks after the wear test, the fluorine reduction is observed only during a short period of several hours after the wear. It seems that the chemically modified carbon remains in the wear track and is later covered by unmodified lubricant flowing over the track from its sides [40].

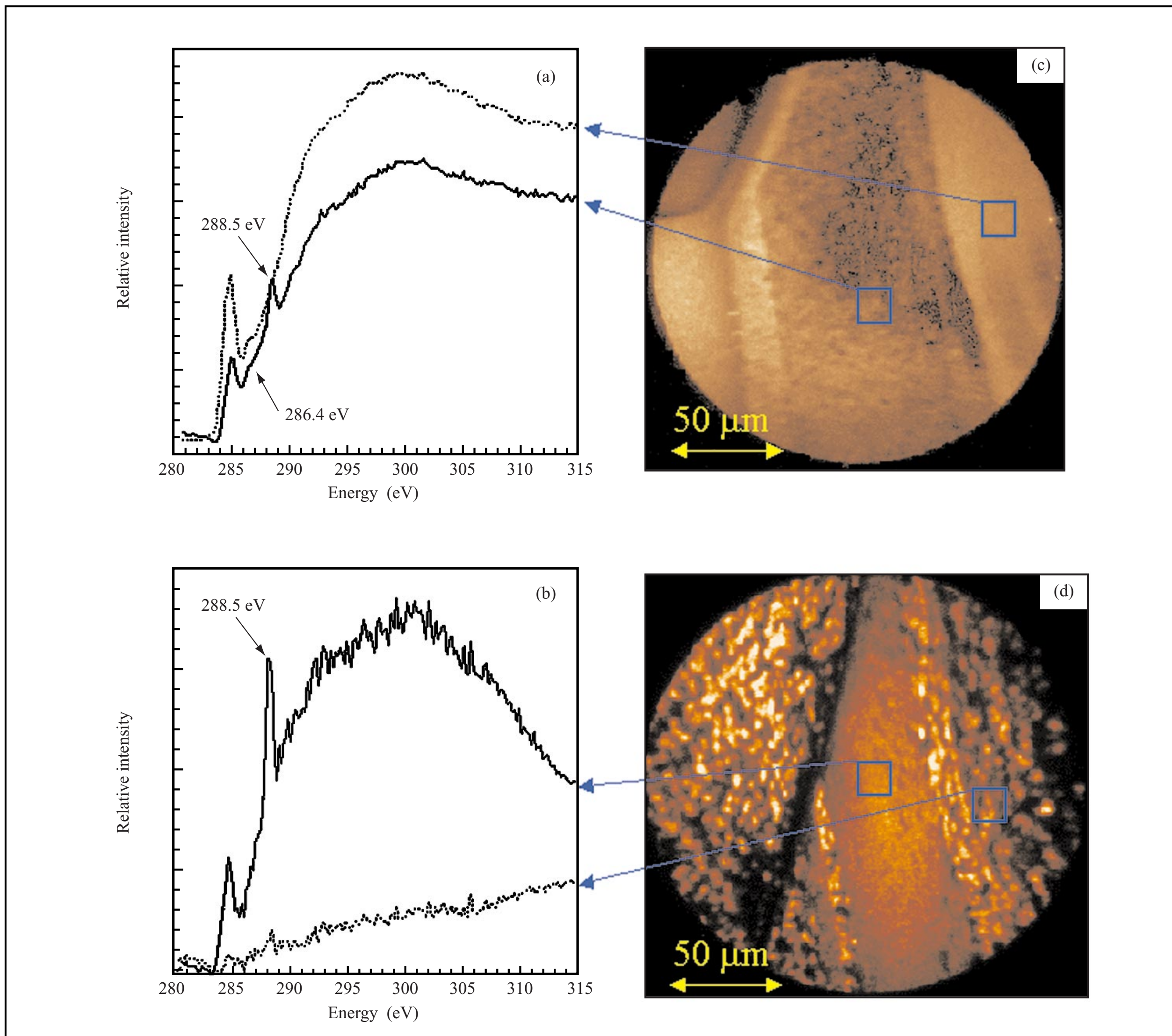

Figure 9

(a) Carbon *K*-edge spectra obtained from within and outside scratch marks on a CH_x-coated slider whose image is shown in (c). (b) Carbon *K*-edge spectra obtained from within and outside scratch marks on the uncoated slider, whose image is shown in (d). Adapted from [39], with permission.

We observe the formation of carboxylic bonds in wear tracks of disks coated with various lubricants, for disks worn in air and in vacuum, and for coated as well as uncoated sliders [39, 40]. Therefore, lubricant oxidation appears to be a very general process during wear occurring under various conditions. Unlubricated disks worn in air or vacuum do not show any chemical modifications (no formation of new bonds) but rather a reduction of the carbon overcoat thickness. Our studies show that, in general, the chemical modification in wear tracks is correlated with the presence of the lubricant and consists of fluorine removal and carbon oxidation.

- *Slider surfaces*

The sliders used in the wear tests described in the previous section were studied as well, using PRISM to detect elemental and chemical modifications of the slider surfaces caused by the wear [39]. First, the sliders were

inspected using an optical microscope after the wear tests. Scratch marks were found on both coated and uncoated sliders. The areas containing the scratches were studied using XPEEM. Local NEXAFS spectra were taken at the surface of a CH_x-coated slider and an uncoated slider inside and outside the scratch marks. The carbon *K*-edge spectra shown in **Figures 9(a)** and **9(b)** are normalized to the incident X-ray flux, and their relative intensity reflects the relative amount of carbon present at the sample surface. The spectrum outside the scratch of the coated slider [Figure 9(a)] is again a typical diamondlike carbon spectrum with the π^* resonance at 285 eV, the broad σ resonance around 300 eV, and a small C=O peak at 286.4 eV. The small oxygen contamination is caused either by oxygen (bulk) contamination during the sputtering process or by surface contamination from air exposure. The spectrum of the uncoated slider outside the scratch in Figure 9(b) shows no carbon signal. The spectra inside the scratches on both the coated and uncoated sliders show a strong carbon signal with an additional strong peak at 288.5 eV, which indicates carboxylic bonds. This is remarkable because the spectrum obtained from within the scratch is very similar to the spectra obtained from within wear tracks of the lubricated disk of Figure 8. The reduction in the carbon signal of the coated slider indicates removal of the coating, and spectra from within the scratches of both coated and uncoated sliders show that degraded, oxidized lubricant has been transferred to the sliders. The carboxylic peak is higher for the uncoated slider, probably because the carbon spectrum of the coated slider is a superposition of the remaining carbon overcoat and the transferred lubricant.

On sliders which were worn on unlubricated disks, only local reduction of the carbon overcoat thickness was observed (reduction in the carbon *K*-edge signal and increase in the titanium *L*-edge signal from the slider bulk material). The carbon signal did not show the peak connected to the formation of carboxylic bonds that is typical for degraded lubricant.

The examples shown in the previous two sections demonstrate the ability to detect elemental and chemical differences on disks and slider surfaces with high spatial resolution, making it possible to identify the chemical reactions which occur in the lubricant during wear and to demonstrate that (at least in the cases studied here) primarily degraded lubricant is transferred from the disk to the sliders and accumulated in scratches.

- *Antiferromagnetic exchange bias materials*

A technologically important phenomenon, used in the manufacturing of magnetic recording heads [42–45] and in the development of magnetic random-access memory cells [46, 47] is the pinning of the magnetization direction of a ferromagnet by coupling it to an antiferromagnet, an effect referred to as exchange biasing or exchange anisotropy [48].

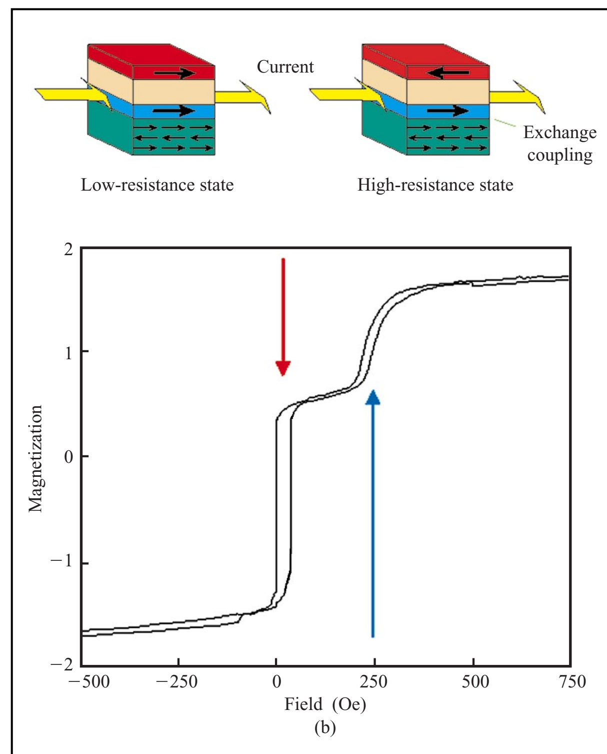

Figure 10

Principle and magnetization loop of a spin valve. The resistance of the spin-valve structure, consisting of an antiferromagnet (green), a hard ferromagnetic layer (blue), a nonmagnetic spacer layer (orange), and a second soft ferromagnetic layer (red), depends on the relative alignment of the two ferromagnetic layers. The magnetization direction of the lower ferromagnetic layer is pinned by exchange coupling to the antiferromagnet, while the magnetization direction in the upper ferromagnetic layer can be readily switched by a weak magnetic field. The magnetization loop of a spin valve of the structure $Mn_{46}Fe_{54}$(100 Å)/Co(40 Å)/AlO_x(14 Å)/$Ni_{40}Fe_{60}$(75 Å) is also shown, revealing the exchange offset loop of the lower ferromagnetic layer (about 250 Oe) and the nearly centered loop of the upper ferromagnetic layer [58].

Of particular importance in the development of ever more sensitive read heads, which sense the small flux changes arising from the magnetic domains on the spinning disk, is the so-called spin-valve head, used in IBM's most advanced disk drives. Its operation is based on the giant magnetic resistance effect. In the spin-valve structure (**Figure 10**), a thin ferromagnetic layer of Co or permalloy, $Ni_{80}Fe_{20}$ (several nm thick, depicted in blue), is grown directly on an antiferromagnetic layer (green), typically FeMn, NiMn, or NiO [42–45]. Its magnetization direction is pinned in a well-defined direction by application of a magnetic field during growth. A second

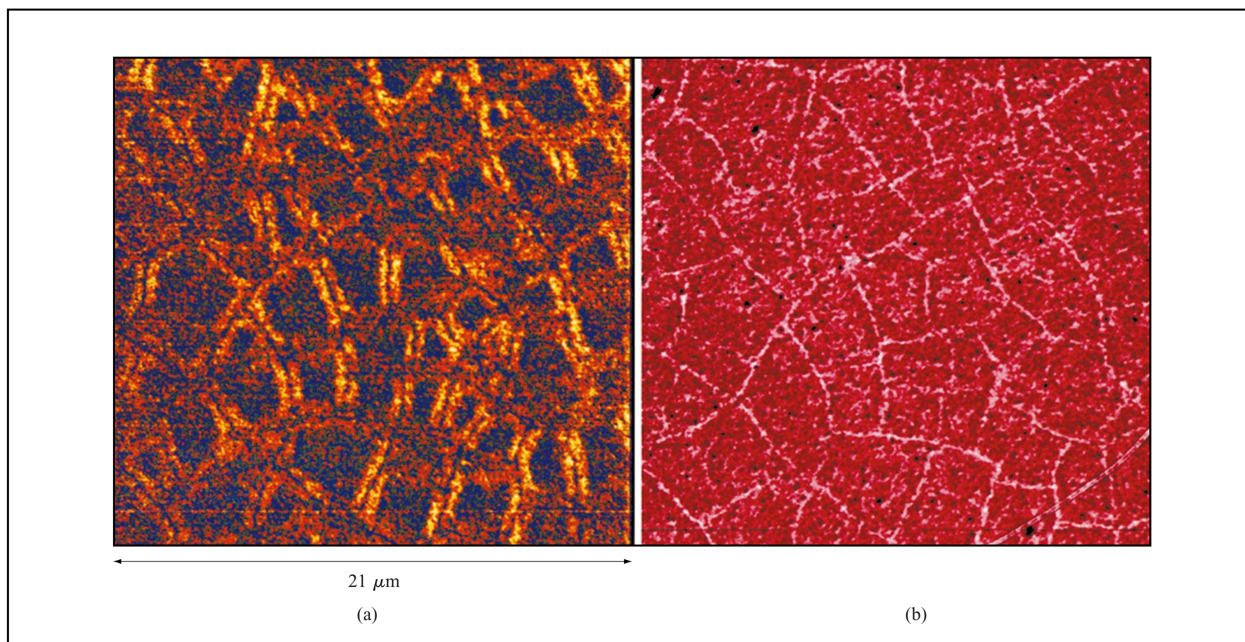

Figure 11

Antiferromagnetic (a) and topographical (b) images of a 400-nm-thick polycrystalline NiO film annealed at 1100°C.[1]

magnetic layer (red) is decoupled from the first one by a thin (a few nm thick) Cu layer, and the magnetization direction of the second magnetic layer may be rotated by the weak magnetic field (about 20 Oe) from magnetized regions of the recording disk. In contrast, the magnetization direction in the pinned blue layer remains unchanged in such weak fields. The change in resistance between parallel and antiparallel alignment of the magnetization directions in the two ferromagnetic layers affects the sensor signal in the spin-valve head. The exchange coupling is reflected by the hysteresis loop shown in Figure 10. While the upper ferromagnetic layer switches in a small field, the loop of the lower ferromagnetic layer is offset from zero field by the exchange field (about 250 Oe in Figure 10). The pinning effect of the magnetization through exchange bias is one of the fundamental requirements for reliable head performance.

Several models have been proposed to explain the exchange biasing effect [49–51], but the difficulty in obtaining experimental information on the magnetic structure at the ferromagnetic/antiferromagnetic interface has prevented a satisfactory understanding. In practice, polycrystalline antiferromagnets are used, since they exhibit larger exchange bias than single-crystal materials. Of particular interest in such materials is the correlation between the crystallographic domain size and the antiferromagnetic domain size. Because of the small size of the grains and domains, the desired information has eluded us so far. At present the spatial resolution of neutron diffraction topography is limited to about 70 μm and that of X-ray diffraction topography to 1–2 μm [52]. The resolution of optical methods such as birefringence [53] or second-harmonic measurements [54] has a fundamental limitation set by diffraction (about 0.2 μm), but in practice larger values, in the tens-of-micrometers range, have been demonstrated [53, 54]. Another problem with these techniques is their lack of surface sensitivity, since exchange biasing is clearly an effect related to the magnetic structure of the surface of the antiferromagnet, not of its bulk.

Figure 11 shows the first reported image of the antiferromagnetic domain structure at the surface of a polycrystalline material.[1] The 400-nm-thick polycrystalline NiO sample was deposited by sputter deposition onto oxidized Si and then annealed for one hour at 1100°C in flowing O_2 at atmospheric pressure, followed by one hour at 700°C, and a gradual (four-hour) cooldown to room temperature in flowing O_2. The annealing procedure increased the crystallographic grain size from about 20 nm to 400 nm. The figure compares an

[1] T. Regan et al., unpublished.

antiferromagnetic image, obtained by dividing an image recorded at 871.2 eV [see Figure 2(b)] by one obtained at 870.0 eV, to a topographical image obtained at one energy only [55].

Comparison of the topographical XPEEM image of Figure 11 with images obtained using atomic force microscopy and cross-section transmission electron microscopy indicates that the topographical image reflects the grain structure at the surface. The contrasting mechanism is that illustrated in Figure 4. The tops of the grains are relatively darker and the valleys between the grains relatively lighter. In addition to the fine grain structure, the topographical image also exhibits a weblike structure consisting of continuous light lines. The contrast indicates that these lines correspond to valleys, and we attribute them to fine cracks in the film arising from the annealing process.

The antiferromagnetic image of Figure 11 consists of bright double lines which are predominantly oriented vertically. The widths of the bright lines are rather uniform and correspond to the grain size in the topographical image. Close inspection reveals that the bright lines follow the weblike pattern in the topographical image, except that no significant antiferromagnetic contrast exists along the horizontal or near-horizontal web lines.

The antiferromagnetic contrast arises from preferential orientation of the antiferromagnetic axis relative to the electric field vector, as illustrated in Figure 2(b). To obtain the images of Figure 11, the electric field vector was oriented parallel to the image plane in the horizontal direction. Bright contrast corresponds to regions with their antiferromagnetic axis oriented *parallel* to the electric field vector. Hence, the bright double stripes in Figure 11(a) correspond to grains adjacent to the cracks which have a preferred in-plane horizontal orientation of the antiferromagnetic axis. Dark contrast corresponds to an antiferromagnetic axis orientation perpendicular to the electric field vector. The image is readily explained by a preferential orientation of the antiferromagnetic axis perpendicular to the cracks. The horizontal crack lines lead to a preferential vertical in-plane orientation of the antiferromagnetic axis, and vertical crack lines lead to a preferential horizontal in-plane orientation of the antiferromagnetic axis.

Figure 11 clearly demonstrates the capabilities of X-ray magnetic linear dichroism microscopy for the study of antiferromagnetic surfaces. Future studies will focus on the correlation between the antiferromagnetic domain structure and the ferromagnetic domain structure in exchange-biased junctions. Such studies will utilize the elemental specificity of X-rays to distinguish the antiferromagnetic (e.g., NiO) layer from the ferromagnetic (e.g., Fe or Co) layers and X-ray polarization contrast to

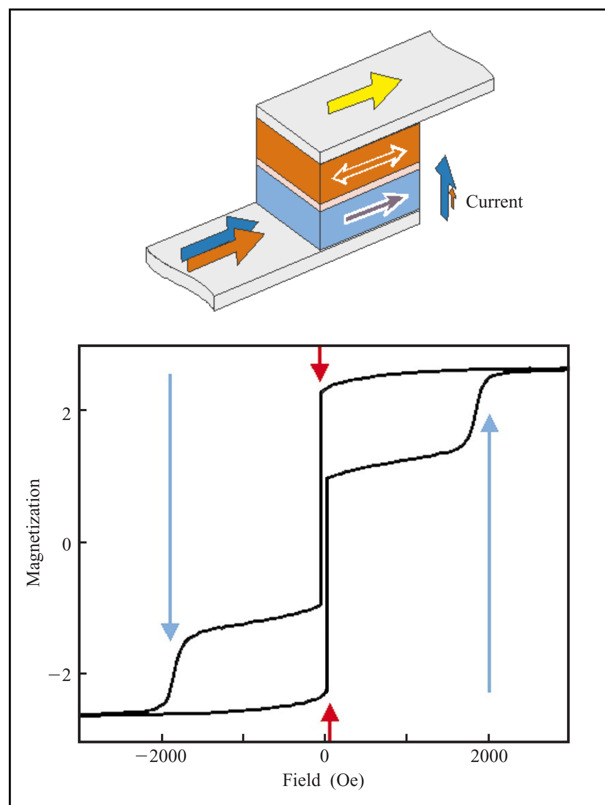

Figure 12

Magnetic tunnel junction and magnetization loop. The blue "hard" layer in the tunnel junction has a large coercivity, while the red "soft" layer has a small coercivity and can be easily rotated, e.g., by the magnetic field created by the current through a nearby write line. The magnetization loop was obtained from a tunnel junction having a $Co_{75}Pt_{12}Cr_{13}$(150 Å)/AlO_x(14 Å)/Co(150 Å) structure; switching fields (coercivities) for the red and blue layers are indicated [58].

image antiferromagnetic domains (linear polarization) and ferromagnetic domains (circular polarization). In the next section we give an example of the use of circularly polarized X-rays for the imaging of ferromagnetic domains.

- *Magnetic tunnel junctions*

In comparison to conventional dynamic random-access memory, which is based on capacitive charge retention, magnetic memory is inherently nonvolatile and does not require periodic refreshing [56]. In principle, a magnetic memory cell could have a spin-valve-like structure where the "ones" and "zeros" correspond to different magnetization directions of the red layer of Figure 10. However, recently tunnel junctions [57] have shown magnetoresistance effects larger (about 30%) than spin valves (about 10%), and such devices are now under consideration at IBM.

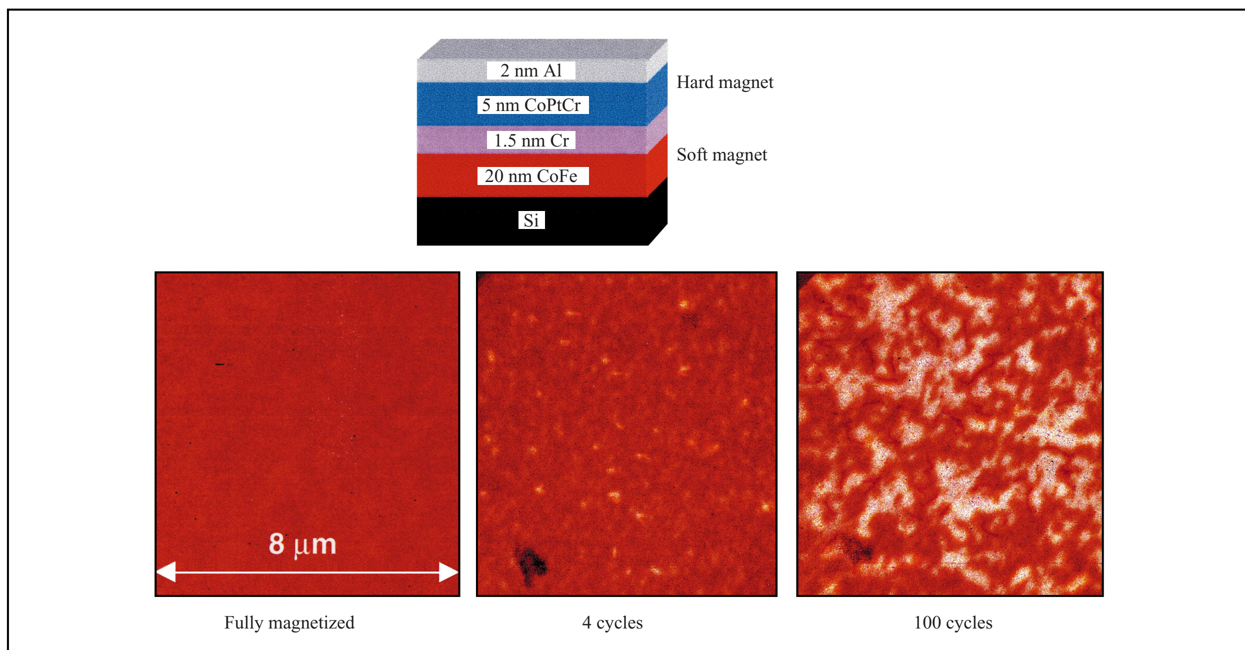

Figure 13

PEEM images of the domain structure of the hard CoPtCr layer in the structure shown, as a function of the number of switching cycles of the soft layer in a field of about 50 Oe [59].

In the magnetic tunnel junction illustrated in **Figure 12**, the thin nonmagnetic layer (e.g., Cu) shown in orange in Figure 10 is replaced by a thin insulator (e.g., aluminum oxide), shown in pink, and the tunnel current flows in a direction perpendicular to the layers. As in the spin valve, the magnetoresistance of the structure depends on the relative orientation of the magnetization in the two ferromagnetic layers, again shown in red and blue in Figure 12. The conceptually simplest way to keep the magnetization in the blue layer fixed is to choose a magnetically hard material such as CoPtCr, which is also used as the storage medium in magnetic disk drives. For the red layer one chooses a magnetically soft material such as permalloy, $Ni_{80}Fe_{20}$. A typical magnetization loop of such a hard/soft magnetic tunnel junction is shown in Figure 12 [58]. It is seen that the red layer may be switched by a magnetic field of tens of oersteds (Oe), while the blue layer requires a field of nearly 2000 Oe for reversal of its magnetization direction.

Unfortunately, in practice, the simple concept shown in Figure 12 does not work as expected [58]. Repeated switching of the soft red layer, which is a fundamental requirement for a memory cell, degrades the performance of the cell until it ceases to function altogether after thousands of cycles. This rather interesting yet devastating effect surprisingly happens in a field more than an order of magnitude smaller than that needed for switching of the blue layer. At first examination, it is therefore difficult to see how the magnetic structure of the blue layer could be responsible for the device deterioration.

The solution to the puzzle is shown in **Figure 13** [59]. Here we show magnetic circular dichroism images of the magnetic domain structure in the hard magnetic layer as a function of switching cycles of the soft magnetic layer in a field of about 50 Oe. For our experiments we utilized the structure shown in the upper half of Figure 13. For the soft layer we used a 20-nm-thick CoFe alloy film, and for simplicity we replaced the oxide layer in a typical tunnel junction with a thin Cr layer. The 5-nm-thick hard CoPtCr layer was covered by a 2-nm-thick Al capping layer to prevent oxidation. For the XMCD images the sample was oriented with the preset magnetization direction in the blue layer antiparallel to the X-ray helicity. Images taken at the Co L_3 edge were divided by those taken at the L_2 edges [Figure 2(c)] so that a fully magnetized sample would appear dark. The image of the untreated sample indeed showed a nearly uniform darkness (Figure 13). However, with an increasing number of cycles the image became nonuniform, indicating the formation of magnetic domains. The size of the bright domains increased with an

increasing number of cycles until an equal number of domains with magnetization direction parallel and antiparallel to the X-ray helicity was observed. Clearly, the hard layer no longer contained a well-defined direction.

As discussed in detail elsewhere [59], the degradation of the hard layer arises from dipolar fields emanating from domain walls in the soft layer. Owing to the small separation of the soft and the hard layers, these local fields may be of the order of 2000 Oe and can locally lead to the switching of the magnetization direction, i.e., the formation of domains. At present, these effects prevent use of the simple structure shown in Figure 12 in magnetic memory cells. Instead, the hard layer is still pinned by exchange biasing.

Conclusions and future outlook

This paper has covered the principles of XPEEM and has presented examples of studies of a variety of materials-related phenomena. From these examples it is clear that XPEEM is a powerful new technique for the characterization of complex materials and their surfaces. The paper would be incomplete without presenting an outlook for the future. While the existing PEEM2 microscope is already capable of providing uniquely new information, such as the antiferromagnetic domain structure of a surface, several instrumental advances are bound to create even more exciting possibilities. Bending magnet synchrotron sources will be replaced by insertion device sources that offer variable X-ray polarization (e.g., horizontal and vertical linear polarization) and higher flux densities. New PEEM instruments will include aberration-correcting optics or energy filters which will significantly reduce chromatic aberrations. With such instruments, spatial resolutions near 2 nm may be possible [20]. Finally, time-dependent microscopy studies will be carried out. Such studies typically will involve pump-probe experiments, in which the time dependence of nonequilibrium parameters, e.g., of the magnetization, are probed by means of the synchrotron pulses. Estimates show that it may thus be possible to obtain snapshots with about a 50-ps time resolution using an image accumulation time of only a few seconds.

Acknowledgments

We would like to thank all of our collaborators in the original work reviewed here. Particular thanks are due to Howard Padmore and Mike Scheinfein, without whom the PEEM2 instrument would not exist. We are also indebted to Andreas Scholl and Jan Luening, who largely carried out the magnetic imaging work discussed here. Part of this work was supported by the U.S. Department of Energy, Office of Basic Energy Sciences, under Contract No. DE-AC03-76SF00098.

References

1. B. P. Tonner, G. R. Harp, S. F. Koranda, and J. Zhang, *Rev. Sci. Instrum.* **63,** 564 (1992).
2. J. Stöhr, H. A. Padmore, S. Anders, T. Stammler, and M. R. Scheinfein, *Surf. Rev. Lett.* **5,** 1297 (1998).
3. *X-Ray Absorption: Principles, Applications, Techniques of EXAFS, SEXAFS and XANES*, D. C. Koningsberger and R. Prins, Eds., Wiley, New York, 1988.
4. J. Stöhr, *NEXAFS Spectroscopy*, Springer Series in Surface Sciences, Vol. 25, Springer, New York, 1992.
5. B. T. Thole, G. van der Laan, and G. A. Sawatzky, *Phys. Rev. Lett.* **55,** 2086 (1985); G. van der Laan, B. T. Thole, G. A. Sawatzky, J. B. Goedkoop, J. C. Fuggle, J.-M. Esteva, R. Karnatak, J. P. Remeika, and H. A. Dabkowska, *Phys. Rev. B* **34,** 6529 (1986).
6. G. Schütz, W. Wagner, W. Wilhelm, P. Kienle, R. Zeller, R. Frahm, and G. Materlik, *Phys. Rev. Lett.* **58,** 737 (1987).
7. G. F. Rempfer and O. H. Griffith, *Ultramicrosc.* **27,** 273 (1989).
8. S. Anders, H. A. Padmore, R. M. Duarte, T. Renner, T. Stammler, A. Scholl, M. R. Scheinfein, J. Stöhr, L. Séve, and B. Sinkovic, *Rev. Sci. Instrum.* **70,** 3973 (1999).
9. J. Stöhr and M. Samant, *J. Electron Spectrosc. Rel. Phenom.* **98–99,** 189 (1999).
10. P. Carra, H. König, B. P. Thole, and M. Altarelli, *Physica B* **192,** 182 (1993).
11. J. Stöhr, *J. Electron Spectrosc. Relat. Phenom.* **75,** 253 (1995).
12. D. Alders, J. Vogel, C. Levelut, S. D. Peacor, T. Hibma, M. Sacci, L. H. Tjeng, C. T. Chen, G. van der Laan, B. T. Thole, and G. A. Sawatzky, *Europhys. Lett.* **32,** 259 (1995).
13. B. T. Thole, P. Carra, F. Sette, and G. van der Laan, *Phys. Rev. Lett.* **68,** 1943 (1992).
14. P. Carra, B. P. Thole, M. Altarelli, and X. Wang, *Phys. Rev. Lett.* **70,** 694 (1993).
15. J. Stöhr and H. König, *Phys. Rev. Lett.* **75,** 3748 (1995).
16. J. Stöhr and R. Nakajima, *IBM J. Res. Develop.* **42,** 73 (1998).
17. R. N. Watts, S. Liang. Z. H. Levine, T. B. Lucatorto, F. Polack, and M. R. Scheinfein, *Rev. Sci. Instrum.* **68,** 3464 (1997).
18. B. L. Henke, J. Liesegang, and S. D. Smith, *Phys. Rev. B* **19,** 3004 (1979).
19. G. F. Rempfer, D. M. Desloge, W. P. Skoczylas, and O. H. Griffith, *Microsc. Microanal.* **3,** 14 (1997).
20. R. Fink, M. R. Weiss, E. Umbach, D. Preikszas, H. Rose, R. Spehr, P. Hartel, W. Engel, R. Degenhardt, R. Wichtendahl, H. Kuhlenbeck, W. Erlebach, K. Ihmann, R. Schlögl, H.-J. Freund, A. M. Bradshaw, G. Lilienkamp, Th. Schmidt, E. Bauer, and G. Brenner, *J. Electron Spectrosc. Relat. Phenom.* **84,** 231 (1997).
21. R. Nakajima, J. Stöhr, and Y. U. Idzerda, *Phys. Rev. B* **59,** 6421 (1999).
22. J. Stöhr, Y. Wu, B. D. Hermsmeier, M. G. Samant, G. R. Harp, S. Koranda, D. Dunham, and B. P. Tonner, *Science* **259,** 658 (1993).
23. H. Ade and B. Hsiao, *Science* **262,** 1427 (1993).
24. A. Cossy-Favre, J. Diaz, Y. Liu, H. R. Brown, M. G. Samant, J. Stöhr, A. J. Hanna, S. Anders, and T. P. Russel, *Macromolecules* **31,** 4957 (1998).
25. D. Spanke, V. Solinus, D. Knabben, F. U. Hillebrecht, F. Ciccacci, L. Gregoratti, and M. Marsi, *Phys. Rev. B* **58,** 5201 (1998).
26. A. Scholl, J. Stöhr, J. Luning, J. W. Seo, J. Fompeyrine, H. Siegwart, J. P. Locquet, F. Nolting, S. Anders, E. E. Fullerton, M. R. Scheinfein, and H. A. Padmore, *Science* **287,** 1014 (2000).
27. B. P. Tonner, D. Dunham, T. Droubay, and M. Pauli, *J. Electron Spectrosc. Relat. Phenom.* **84,** 211 (1997).

28. H. Jeon, C. A. Sukow, J. W. Honeycutt, G. A. Rozgony, and R. J. Nemanich, *J. Appl. Phys.* **71,** 4269 (1992).
29. R. A. Roy, L. A. Clevenger, C. Cabral, Jr., K. L. Saenger, S. Brauer, J. Jordan-Sweet, J. Buccignano, G. B. Stephensen, G. Morales, and K. F. Ludwig, Jr., *Appl. Phys. Lett.* **66,** 1732 (1995).
30. K. L. Saenger, C. Cabral, Jr., L. A. Clevenger, R. A. Roy, and S. Wind, *J. Appl. Phys.* **78,** 7040 (1995).
31. S. Singh, H. Solak, N. Krasnoperov, F. Cerrina, A. Cossy, J. Diaz, J. Stöhr, and M. Samant, *Appl. Phys. Lett.* **71,** 55 (1997).
32. H. Ade, X. Zhang, S. Cameron, C. Costello, J. Kirz, and S. Williams, *Science* **258,** 972 (1992).
33. D. Slep, J. Asselta, M. H. Rafailovich, J. Sokolov, D. A. Winesett, A. P. Smith, H. Ade, Y. Strzhemechny, S. A. Schwarz, and B. B. Sauer, *Langmuir* **14,** 4860 (1998).
34. D. A. Winesett, H. Ade, A. P. Smith, M. Rafailovich, S. Sokolov, and D. Slep, *Microsc. Microanal.* **4,** Suppl. 2, 828 (1998).
35. H. Ade, D. A. Winesett, A. P. Smith, S. Anders, T. Stammler, C. Heske, D. Slep, M. H. Rafailovich, J. Sokolov, and J. Stöhr, *Appl. Phys. Lett.* **73,** 3775 (1998).
36. D. Slep, J. Asselta, M. H. Rafailovich, J. Sokolov, D. A. Winesett, A. P. Smith, H. Ade, and S. Anders, *Langmuir* **16,** 2369 (2000).
37. J. Wei, W. Fong, D. B. Bogy, and C. S. Bhatia, *Tribol. Lett.* **5,** 203 (1998).
38. C. S. Bhatia, W. Fong, C.-Y. Chen, J. Wei, D. B. Bogy, S. Anders, Th. Stammler, and J. Stöhr, *IEEE Trans. Mag.* **35,** 910 (1999).
39. S. Anders, T. Stammler, W. Fong, D. B. Bogy, C. S. Bhatia, and J. Stöhr, *J. Vac. Sci. Technol. A* **17,** 2731 (1999).
40. S. Anders, T. Stammler, W. Fong, C.-Y. Chen, D. B. Bogy, C. S. Bhatia, and J. Stöhr, *J. Tribol.* **121,** 961 (1999).
41. X. H. Yun, D. B. Bogy, and C. S. Bhatia, *IEEE Trans. Mag.* **32,** 3669 (1996).
42. R. Hempstead, S. Krongelb, and D. A. Thompson, *IEEE Trans. Mag.* **14,** 521 (1978).
43. C. Tsang, N. Heiman, and K. Lee, *J. Appl. Phys.* **52,** 2471 (1981).
44. C. Tsang, *J. Appl. Phys.* **55,** 2226 (1984).
45. For a review, see S. S. P. Parkin, *IBM J. Res. Develop.* **42,** 3 (1998).
46. J. M. Daughton, *Thin Solid Films* **216,** 162 (1992).
47. D. D. Tang, P. K. Wang, V. S. Speriosu, S. Le, and K. K. Kung, *IEEE Trans. Mag.* **31,** 3206 (1995).
48. W. H. Meiklejohn and C. P. Bean, *Phys. Rev.* **102,** 1413 (1956); W. H. Meiklejohn, *J. Appl. Phys.* **33,** Suppl., p. 1328 (1962).
49. A. P. Malozemoff, *Phys. Rev. B* **35,** 3679 (1987); A. P. Malozemoff, *J. Appl. Phys.* **63,** 3874 (1988).
50. D. Mauri, H. C. Siegmann, P. S. Bagus, and E. Kay, *J. Appl. Phys.* **62,** 3047 (1987).
51. N. C. Koon, *Phys. Rev. Lett.* **78,** 4865 (1997).
52. J. Baruchel, *Phys. B* **192,** 79 (1993).
53. S. Saito, M. Miura, and K. Kurosawa, *J. Phys. C* **13,** 1513 (1980).
54. M. Fiebig, D. Fröhlich, St. Leute, and R. V. Pisarev, *Appl. Phys. B* **66,** 265 (1998).
55. J. Stöhr, A. Scholl, T. J. Regan, S. Anders, J. Luning, M. R. Scheinfein, H. A. Padmore, and R. L. White, *Phys. Rev. Lett.* **83,** 1862 (1999).
56. W. J. Gallagher, S. S. P. Parkin, Y. Lu, X. P. Bin, A. Marley, K. P. Roche, R. A. Altman, S. A. Rishton, C. Jahnes, T. M. Shaw, and G. Xiao, *J. Appl. Phys.* **81,** 3741 (1997).
57. J. S. Moodera, L. R. Kinder, T. M. Wong, and R. Meservey, *Phys. Rev. Lett.* **74,** 3273 (1995).
58. S. Gider, B.-U. Runge, A. C. Marley, and S. S. P. Parkin, *Science* **281,** 797 (1998).
59. L. Thomas, J. Lüning, A. Scholl, F. Nolting, S. Anders, J. Stöhr, and S. S. P. Parkin, *Phys. Rev. Lett*. **84,** 3462 (2000).

Received May 24, 1999; accepted for publication September 10, 1999

Joachim Stöhr *Stanford Synchrotron Radiation Laboratory, P.O. Box 20450, MS 69, Stanford, California 94309 (stohr@ssrl.slac.stanford.edu).* Dr. Stöhr is the Deputy Director of the Stanford Synchrotron Radiation Laboratory and a Professor at Stanford University. While this paper was written, he was a Research Staff Member at the Almaden Research Center, where he is currently a consultant. Dr. Stöhr received a B.S. degree in physics from Friedrich Wilhelms University in Bonn, an M.S. degree in physics from Washington State University (as a Fulbright scholar), and a Ph.D. degree in physics from the Technical University of Munich. In 1975 and 1976 he was a Postdoctoral Fellow at the Lawrence Berkeley National Laboratory; he joined the Stanford Synchrotron Radiation Laboratory as a Staff Scientist in 1977. In 1981 he became a Senior Staff Physicist at the EXXON Corporate Research Science Laboratory. He left EXXON in 1985 to join the IBM Almaden Research Center, where he conducted research in the areas of surface science and magnetic materials and managed the Condensed Matter and the Magnetic Materials and Phenomena departments for several years. Dr. Stöhr joined the Stanford faculty in January 2000. His research in surface science and magnetic materials has focused on the development of novel investigative techniques based on synchrotron radiation for exploring the structure and properties of surfaces and thin films. He played a major role in developing surface extended X-ray absorption fine structure (SEXAFS) as a tool for exploring surface structures. He also developed the near-edge X-ray absorption fine structure (NEXAFS) technique for the study of simple and complex molecules bonded to surfaces and for the study of thin organic (polymeric) films. These two techniques have become widely used. Dr. Stöhr has written definitive reviews of both fields; he is the author of the book *NEXAFS Spectroscopy*. More recently he has turned his attention to the use of polarized X-rays for the study of magnetic phenomena. He has pioneered X-ray magnetic dichroism spectro-microscopy, which makes possible the direct observation of antiferromagnetic and ferromagnetic domain structure with elemental and chemical state specificity. He is the author of more than 230 scientific publications, and he is also an Adjunct Professor in Physics at Uppsala University, Sweden. Dr. Stöhr has been a Fellow of the American Physical Society since 1988 and is currently a member of the Basic Energy Sciences Advisory Committee (BESAC) of the Department of Energy.

Simone Anders *Lawrence Berkeley National Laboratory, 1 Cyclotron Road, MS 2-400, Berkeley, California 94720 (SAnders@lbl.gov).* Dr. Anders is a Staff Scientist at the Lawrence Berkeley National Laboratory; she is joining the IBM Almaden Research Center in July 2000. She studied physics at Humboldt University, Berlin, and plasma physics at Moscow State University, Russia. She holds an M.S. degree (1984) and a Ph.D. degree (1988) in physics, both from Humboldt University. In 1988 Dr. Anders joined the Central Institute of Electron Physics (Berlin), where she investigated electrical breakdown phenomena in vacuum and in gases. In 1992 she joined the Lawrence Berkeley National Laboratory (LBNL), where she worked in the field of vacuum arc plasma and ion source development, vacuum arc deposition, and metal ion implantation. In 1996 she joined the Advanced Light Source facility at the LBNL, where she heads their photoemission electron microscopy (PEEM) project. Dr. Anders is a Senior Member of IEEE and a member of MRS and AVS. She was Chairman of the XVIIth International Symposium on Discharges and Electrical Insulation in Vacuum, Berkeley, 1996. She is an author or co-author of more than 80 publications in refereed journals and holds three patents. In 1994, Dr. Anders received the Chatterton Young Investigator Award for Outstanding Achievement in the Field of Discharges and Electrical Insulation in Vacuum. Her current research interests include the application of X-ray-based analysis techniques to the investigation of magnetic materials and polymers, and the design of electron optical microscopes.